International Journal of Impact Engineering 176 (2023) 104563

Contents lists available at ScienceDirect

International Journal of Impact Engineering

journal homepage: www.elsevier.com/locate/ijimpeng

A non-linear viscoelastic material model with progressive damage based on microstructural evolution and phase transition in polycrystalline ice for design against ice impact

Mojtaba Mokhtari *, Ekaterina Kim, Jørgen Amdahl

Centre for Autonomous Marine Operations and Systems (AMOS), Department of Marine Technology, Norwegian University of Science and Technology (NTNU), Norway

ARTICLE INFO

Keywords:
Ice impact
Rate-dependent material
Material model
Damage model
Viscoelasticity
Multiphysics

ABSTRACT

This study presents a nonlinear viscoelastic material model incorporating a progressive damage framework with an iterative algorithm for glacial/freshwater polycrystalline ice subject to compressive impact load induced by ice-structure interaction. The damage model accounts for microcracking, dynamic recrystallisation, pressure melting, and high-shear elastic failure with a pressure- and rate-dependent convex failure locus. The constitutive laws are written in Fortran and implemented as a vectorised user material (VUMAT) in Abaqus with three different numerical methods, Lagrangian FEM, coupled FEM-SPH, and ALE-FEM. The constitutive model together with the implemented numerical methods are validated against two different types of laboratory-scale physical tests, indentation of cone-shaped ice and triaxial creep. The proposed model implemented with the coupled FEM-SPH method enables simulation of the cyclic transition from solid-like intact ice to the fluid-like pulverised/granular substance, progressively extruded with viscous rheology.

1. Introduction

From space to the Earth's oceans, ice, in its different forms, poses a collision hazard to man-made structures [1–5]. Nevertheless, design against ice impact is still challenging due to incomplete knowledge regarding the behaviour of ice in different environments and engineering applications. This is because ice behaviour is associated with many uncertainties owing to its varied compositional and microstructural properties in different environments, as well as the phase transition and microstructural transformations in different loading conditions. Design against ice actions is of great concern in the maritime sector considering the extensive human activities in icy waters including shipping, natural resource exploration, commercial fisheries, and tourism, that have been on the rise in recent years.

Numerical methods, in particular Finite Element Methods (FEM), are widely used to simulate and study the structural and dynamic behaviour of marine structures subject to ice impact. The accuracy and reliability of these simulations are highly dependent on the ice material model. However, there is still no universal or widely accepted material model for ice given its complex and rather stochastic behaviour. Extensive research has been done to understand the mechanical behaviour of ice in ice-structure collision scenarios. Nevertheless, there are still disagreements on the rheology of ice in marine structure-ice interaction scenarios, especially when ice undergoes high strain rates in collision events [6], for which the material models in the literature could be divided into two main groups in terms of their rheological behaviour, elastoplastic and viscoelastic. Many experimental studies support the viscoelastic behaviour of ice [7–16] in particular when the strain rate is lower than the ductile-to-brittle transition strain rate of ice, reported to be in the range of 10^{-4}–10^{-2} s^{-1} [17–25]. However, plasticity-based material models have been used far more often than viscoelastic models to simulate ice-structure interactions in particular collision scenarios [26]. There are several reasons as to why plasticity models are preferred over viscoelastic models as discussed in [26]. Despite the acceptable performance of plasticity models, there is still some debate on modelling ice with the viscoelastic theory for design against ice impact. This is because, even in high-speed impact scenarios, ice could undergo crushing cycles that involve the regions near the interaction interface crushed into a dense pulverised layer extruding with the viscous flow. The energy taken for the extrusion of this viscous substance is believed to be significant enough to affect the reaction force magnitude and oscillation pattern [16,27]. Also, simulating the extruding material could affect the contact area, thereby changing the reaction force profile. However, the literature is lacking finite element models

* Corresponding author.
E-mail address: mojtaba.mokhtari@ntnu.no (M. Mokhtari).

https://doi.org/10.1016/j.ijimpeng.2023.104563

Available online 6 March 2023
0734-743X/© 2023 The Author(s). Published by Elsevier Ltd. This is an open access article under the CC BY license (http://creativecommons.org/licenses/by/4.0/).

that could simulate the extruding material with the viscous flow in multiple crushing cycles as either the finite elements are deleted from the analysis before undergoing significant deformations or only one cycle of the crushing is simulated due to the numerical challenges. Therefore, a viscoelastic material model with progressive damage incorporating an iterative algorithm is developed herein as a vectorized user material (VUMAT) in FORTRAN for Abaqus 2019 [28] to simulate multiple crushing cycles of ice including the extrusion of the highly damaged viscous substance.

The cone-shaped ice crushing tests with a flat indenter carried out by Kim et al. [29] are adopted to validate the viscoelastic material model presented in this study. These tests [29] have been commonly used in several studies to validate the ice material models employed for ice-structure interactions (e.g., [26,29-36]) for several reasons, including the accessibility of the information required for the numerical modelling of the tests. Besides, major spalling does not usually occur in the cone-shaped ice crushing tests which provides a good condition for validating the continuum mechanics-based material models such as those in [26] and the viscoelastic model presented herein. It is worth noting that natural ice samples incorporate several uncertainties such as inconsistent defects (large-scale unhealed cracks) and bubble densities/distributions and may not be ideal for first-line validation of the material models. On the contrary, laboratory-produced ice samples follow a standard preparation process ensuring consistent repeatable ice quality and crushing force results. Details of the cone-shaped ice crushing tests and other physical tests simulated herein to validate the viscoelastic material model are discussed in Section 3.

2. Ice mechanics and viscoelasticity

In a pioneering study, Glen [37] investigated the creep behaviour of polycrystalline ice by applying 1 to 10 bars compressive stresses on ice blocks with temperatures in the range of -13°C to the melting point of ice. He proposed a power-law relation between the viscous/creep strain rate (termed 'minimum flow rate' in his study) and stress,

$$\dot{\varepsilon}^c = B\exp(-Q/RT)\sigma^n \tag{1}$$

where σ and $\dot{\varepsilon}^c$ are stress and the creep strain rate of polycrystalline ice under uniaxial compression, respectively; B and n are constants, Q is the activation energy, $R = 8.314$ J/molK is the universal gas constant, and T is the absolute temperature in degrees Kelvin. The power-law in Eq. (1) has been endorsed in several investigations (e.g., [38–40]).

In 1978, Sinha [8] developed a Burgers-type viscoelastic model for columnar-grained ice under uniaxial compressive load, normal to the columns. The total strain, ε, in his model was decomposed to three components, one instantaneous elastic component and two creep components so that

$$\varepsilon = \varepsilon^e + \varepsilon^d + \varepsilon^c \tag{2}$$

where ε^e is the 'instantaneous elastic' strain; ε^d and ε^c are the creep strain components termed 'delayed elastic' or 'recoverable primary creep' strain, and the 'permanent viscous' or 'secondary creep' strain. These components are outlined in Fig. 1. For clarity, ε^e, ε^d, and ε^c are henceforth termed 'instantaneous elastic strain', 'delayed elastic strain', and 'secondary creep strain', respectively. Based upon Glen's law [37], Sinha [8] utilized the following power-law relation to define the secondary creep strain rate in columnar-grained ice.

$$\dot{\varepsilon}^c = \dot{\varepsilon}_0^c\left(\frac{\sigma}{\sigma_0}\right)^m \tag{3}$$

where $\dot{\varepsilon}_0^c$ is the reference secondary creep strain rate for unit stress (i.e., σ_0=1 MPa), and m is a constant. Sinha [8] also developed an expression for the delayed elastic strain,

$$\varepsilon^d = c\left(\frac{\sigma}{E}\right)^{\varsigma}\left[1-\exp\left\{-(a_T t)^b\right\}\right] \tag{4}$$

where c, ς, a_T, and b are constants; E and t are elastic modulus and time, respectively. Later, he modified this expression for polycrystalline ice [41] to include the grain size effect by replacing c with a grain size dependent term, $c_1(d_1/d)$, where c_1=9 is a constant corresponding to the unit grain diameter (i.e., d_1=1 mm) and d is the grain diameter. Jordaan and McKenna [42] extended Sinha's model to a strict Burgers model (Fig. 1) with a nonlinear stress-dependent dashpot in the Kelvin unit so that

$$\varepsilon^d = \frac{\sigma}{E_K}\left[1-\exp\left\{-\int_0^t \frac{E_K}{\mu_K(\sigma_d)}dt\right\}\right] \tag{5}$$

where E_K and μ_K are the elastic modulus of the spring and the viscosity of the dashpot in the Kelvin unit, respectively.

The nonlinear viscoelastic model proposed by Jordaan and McKenna [42,43], which accounted for microstructural changes in crushing ice through a damage model based on Schapery's continuum damage theory [44,45], has been expanded in several studies (e.g., [12,46-50]). Based upon Jordaan and McKenna [42,43,51] and Jordaan et al. [27], Xiao [12] modelled the viscoelastic behaviour of ice with Eqs. (6)–(24). In Xiao's study [12], the total strain rate is composed of instantaneous elastic strain rate, delayed elastic strain rate, and secondary creep strain rate,

$$\dot{\varepsilon}_{ij} = \dot{\varepsilon}_{ij}^e + \dot{\varepsilon}_{ij}^d + \dot{\varepsilon}_{ij}^c \tag{6}$$

where $\dot{\varepsilon}_{ij}$, $\dot{\varepsilon}_{ij}^e$, $\dot{\varepsilon}_{ij}^d$, and $\dot{\varepsilon}_{ij}^c$ are the total, instantaneous elastic, delayed elastic, and secondary creep strain rate tensors. Having the delayed elastic and secondary creep strains decomposed to deviatoric and volumetric parts, Eq. (6) can be rewritten as

$$\dot{\varepsilon}_{ij} = \dot{e}_{ij}^e + \dot{e}_{ij}^d + \dot{e}_{ij}^c + \dot{\varepsilon}^v\delta_{ij} \tag{7}$$

where $\dot{e}_{ij}^d$ and $\dot{e}_{ij}^c$, defined by Eqs. (8) and (9), are the deviatoric parts of the delayed elastic and secondary creep strain rate tensors; δ_{ij} is the Kronecker delta, and $\dot{\varepsilon}^v$ is the inelastic volumetric strain rate given by Eq. (10). $\dot{\varepsilon}^v$ accounts for the dilatation of ice undergoing cracking and

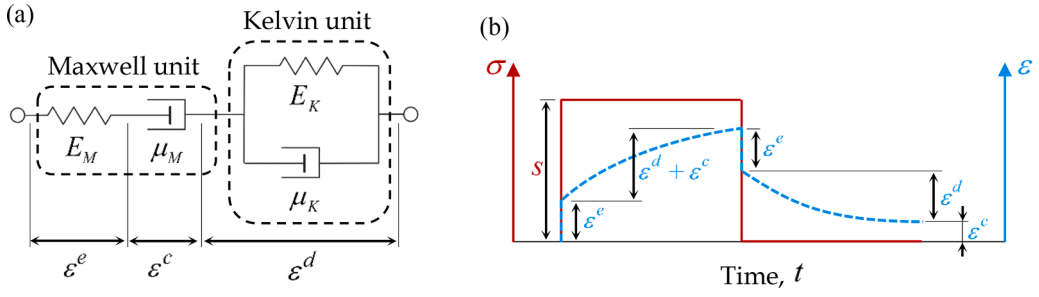

Fig. 1. Burgers material; (a) body diagram; (b) typical strain response (blue dashed line) to constant stress (red solid line). Note s is the von Mises stress.

pulverization and also the compaction and sintering of crushed ice under high confining pressure [11,12,52-54].

$$\dot{e}_{ij}^{d} = \frac{3}{2}\frac{s_{ij}}{\mu_K} \tag{8}$$

$$\dot{e}_{ij}^{c} = \frac{3}{2}\frac{s_{ij}}{\mu_M} \tag{9}$$

$$\dot{\varepsilon}^{v} = \frac{f_3}{p}s(\dot{e} - \dot{e}^{e}) = \frac{f_3}{p}s\left(\dot{e}^{d} + \dot{e}^{c}\right) \tag{10}$$

where s_{ij} is the deviatoric stress tensor; μ_M is the viscosity of the dashpot in the Maxwell unit; $\dot{e}$ is the total equivalent strain rate composed of instantaneous elastic, $\dot{e}^{e}$, delayed elastic, $\dot{e}^{d}$, and secondary creep, $\dot{e}^{c}$, components; s is the von Mises stress; f_3 is a constant and p is the hydrostatic pressure. The viscosities of the Kelvin and Maxwell units in [12] were defined by

$$\mu_K = \frac{s}{\dot{\varepsilon}_0^{d}}\left(\frac{\sigma_0}{s - E_k e^{d}}\right)^{n} \tag{11}$$

$$\mu_M = \frac{s}{\dot{\varepsilon}_0^{c}}\left(\frac{\sigma_0}{s}\right)^{m} \tag{12}$$

where $\dot{\varepsilon}_0^{d}$ and $\dot{\varepsilon}_0^{c}$ are the reference delayed elastic and secondary creep strain rates; σ_0 is the reference stress; n and m are constants, and e^{d} is the equivalent delayed strain expressed by

$$e^{d} = \int_0^{t} \dot{e}^{d} dt \tag{13}$$

Substituting Eq. (11) in Eq. (8) and Eq. (12) in Eq. (9) yields

$$\dot{e}_{ij}^{d} = \frac{3}{2}\dot{\varepsilon}_0^{d}\left(\frac{s - E_k e^{d}}{\sigma_0}\right)^{n}\frac{s_{ij}}{s} \tag{14}$$

$$\dot{e}_{ij}^{c} = \frac{3}{2}\dot{\varepsilon}_0^{c}\left(\frac{s}{\sigma_0}\right)^{m}\frac{s_{ij}}{s} \tag{15}$$

According to [12,13], microstructural damage in ice can be modelled by multiplying an exponential term in the creep strain rates so that

$$\dot{e}_{ij}^{d} = \frac{3}{2}\dot{\varepsilon}_0^{d}\left(\frac{s - E_k e^{d}}{\sigma_0}\right)^{n}\frac{s_{ij}}{s}\exp(\beta_d \mathrm{S}) \tag{16a}$$

$$\dot{e}_{ij}^{c} = \frac{3}{2}\dot{\varepsilon}_0^{c}\left(\frac{s}{\sigma_0}\right)^{m}\frac{s_{ij}}{s}\exp(\beta_c \mathrm{S}) \tag{17}$$

where β_d and β_c are constants known as creep enhancement factors/parameters and S is the damage index function. Xiao [12] gave the following formulation for S based on the investigations carried out in [13,44,45,51,54-56].

$$\mathrm{S} = \mathrm{S}_1 + \mathrm{S}_2 = \int_0^{t}\left\{f_1(p)\left(\frac{s}{s_0}\right)^{q_1} + f_2(p)\exp\left(\frac{s}{s_0}\right)\right\}dt \tag{18a}$$

$$f_1(p) = \begin{cases} a_1\left(1 - \dfrac{p}{p_1}\right)^{2} & p < p_1 \\ 0 & p \geq p_1 \end{cases} \tag{19a}$$

$$f_2(p) = a_2\left(\frac{p}{p_2}\right)^{r} \tag{20}$$

where q_1, a_1, a_2, p_1, p_2, and r are constants, and s_0 is the reference stress of the damage model. For clarity, this damage model, defined by Eqs. (18a), Eq. (19a) and Eq. (20), is termed 'DMa' in this study, where DM stands for Damage Model. In Eq. (18a), S is comprised of two parts, S_1 and S_2. The microcracking damage is modelled by S_1 while S_2 takes the pressure softening processes such as dynamic recrystallisation and pressure melting into account. In the absence of these microstructural changes, S is zero meaning that the exponential damage terms in Eqs. (16a) and (17) are ineffective (i.e., exp(0)=1).

After $\dot{e}_{ij}^{d}$, $\dot{e}_{ij}^{c}$, and $\dot{\varepsilon}^{v}$ are computed using Eqs. (16a), (17), and (10) in an explicit solver, the instantaneous elastic strain rate, $\dot{\varepsilon}_{ij}^{e}$, is found from Eq. (7), which is employed in stress increment, $\Delta\sigma_{ij}$, calculations,

$$\Delta\sigma_{ij} = D_{ijkl}\Delta\varepsilon_{ij}^{e} + \Delta D_{ijkl}\varepsilon_{ij}^{e} \tag{21}$$

$$\Delta\varepsilon_{ij}^{e} = \dot{\varepsilon}_{ij}^{e} dt \tag{22}$$

$$\varepsilon_{ij}^{e} = \frac{1+\nu}{E_M}\sigma_{ij} - \frac{\nu}{E_M}\sigma_{kk}\delta_{ij} \tag{23}$$

where ε_{ij}^{e} and σ_{ij} are respectively the instantaneous elastic strain and the Cauchy stress tensors, and σ_{kk} is the sum of normal stresses; ν and E_M are respectively the Poisson's ratio and the Maxwell spring stiffness (simulating the instantaneous elastic response of ice); D_{ijkl} is a component in the isotropic elastic stiffness tensor, $\mathbb{D}$, that is a fourth-order tensor with minor symmetry (i.e. $D_{ijkl} = D_{jikl} = D_{ijlk} = D_{jilk}$). Using the elastic damage relation of Kachanov [57], ΔD_{ijkl} is expressed by

$$\Delta D_{ijkl} = \frac{D_{ijkl}^{0}}{1 + C(S + \Delta S)} - \frac{D_{ijkl}^{0}}{1 + CS} \tag{24}$$

where the superscript ^{0} is the initial state index, and C is a proportional constant that is equal to one according to [49]. Eq. (24) is a simplified form of a more general formulation (see [11,12] for more information), which is valid only if $C_1 = C_2 = C$ in

$$E = E^{0}(1 + C_1 S)^{-1} \tag{25}$$

$$G = G^{0}(1 + C_2 S)^{-1} \tag{26}$$

where C_1 and C_2 are constants, and$G$ is the shear modulus.

Two recent studies [50,58] have reported that the viscoelastic model with the constitutive equations listed above Eqs. (6)–((24)) could produce unrealistically large stresses in numerical simulations. Shi et al. [58] reported that although the viscoelastic model well simulates compressive creep tests with relatively low and moderate strain rates, it might overestimate the ice strength in iceberg-ship collision scenarios where much higher strain rates due to short loading durations (0.01–1.0 s) are induced. It was argued that the viscoelastic model does not account for the ductile to brittle transition so that the stress continues to increase exponentially with the strain rate even for the strain rates beyond the transition strain rate while the ice strength is shown to remain almost constant [17,18] upon a transition strain rate, ≈ 0.002 s^{-1}. Recently, Turner [50] conducted a detailed and comprehensive study on the viscoelastic material model outlined above Eqs. (6)–((24)). He found that the viscoelastic model, implemented with FEM, occasionally produced von Mises stresses significantly larger than those measured in his physical tests. The strength of ice samples in the physical tests — triaxial tests on cylindrical specimens of granular ice prepared according to Stone et al. [59] — was found to remain under a certain value at which the samples failed. This upper limit of the ice strength, expressed with an equivalent (von Mises) stress of 26.0 ± 1.6 MPa, was found to be associated with 'high-shear elastic failure' phenomenon. Turner examined four different models to describe and numerically implement the high-shear elastic failure (HSEF),

$$\text{HSEF1}: \ \sigma_{ij} = \begin{cases} \sigma_{ij} & s \leq 26 \text{ MPa} \\ \sigma_{ij}\dfrac{26}{s} & s > 26 \text{ MPa} \end{cases} \tag{27}$$

$$\text{HSEF2}: \ S_1 = \begin{cases} S_1 & s \le 26 \text{ MPa} \\ S_{max} & s > 26 \text{ MPa} \end{cases} \tag{28}$$

$$\text{HSEF3}: \ E_M = \begin{cases} E_M & s \le 26 \text{ MPa} \\ E_M \dfrac{26}{s} & s > 26 \text{ MPa} \end{cases} \tag{29}$$

$$\text{HSEF4}: \ E_M = \begin{cases} E_M & s \le 26 \text{ MPa} \\ \dfrac{E_M}{100} & s > 26 \text{ MPa} \end{cases} \tag{30}$$

HSEF1, enforcing a limit of 26.0 MPa on the von Mises stress, could not replicate the experimental results as it produced force-displacement (*F-D*) curves insensitive to the strain rate. Besides, this model could not develop the damage layer commonly observed in ice crushing tests. Consequently, HSEF1 was discarded [50]. The second model, HSEF2, suggests that the microcracking damage function, S_1, in an element immediately reaches an upper limit, S_{max}=14.0, if the von Mises stress in that element exceeds the 26.0 MPa threshold. This model was also dismissed in part because it resulted in a sharp load drop with a dramatic increase in the size of the damage layer in just 0.002 s (due to the abrupt jump in the value of S_1 to 14.0) while the damage layer development should be a continuous process according to experimental observations in ice indentation tests. The last two models, HSEF3 and HSEF4, reduce the elastic modulus when the von Mises stress exceeds the 26.0 MPa threshold, and this reduction is independent of the microstructural damage (i.e., microcracking/dynamic recrystallization). HSEF3 gradually reduces the elastic modulus by scaling it down in any time step that s exceeds 26.0 MPa, while HSEF4 enforces a sudden drastic drop on the elastic modulus a single time, by a factor of 100. Although HSEF3 and HSEF4 produced more satisfactory results than the first two models (i.e., HSEF1 and HSEF2), they contradict the theory of 'constant elastic modulus' established and validated earlier in Turner's thesis [50] before investigating the HSEF effect. Besides, the physical meaning of HSEF3 and HSEF4 models is unclear. Therefore, further theoretical and experimental work was recommended to better understand and numerically implement the high-shear elastic failure [50]. The delayed strain rate and the damage model were also expressed slightly differently in [50] by

$$\dot{e}_{ij}^{d} = \frac{3}{2}\dot{\varepsilon}_0^{d}\,\mathrm{sgn}\left(s - E_k e^{d}\right)\left(\frac{\left|s - E_k e^{d}\right|}{\sigma_0}\right)^{n}\frac{s_{ij}}{s}\exp(\beta_d S) \tag{16b}$$

$$S = S_1 + S_2 = \int_0^t \left\{ f_1(p)\left(\frac{s}{s_0}\right)^{q_1} + f_2(p)\left(2^{s/s_0} - 1\right)\right\} dt \tag{18b}$$

$$f_1(p) = a_1 \exp\left(-\frac{p}{p_1}\right) \tag{19b}$$

where sgn(•) is the sign function. This relatively different damage model defined by Eq. (18b), Eq. (19b), and Eq. (20) is henceforth termed 'DMb'.

The present study aims to present a nonlinear viscoelastic constitutive model for simulating glacial/freshwater polycrystalline ice-structure collision with repeating cycles of crushing and viscous extrusion of ice. For this purpose, a combination of the constitutive equations presented by Xiao [12] and Turner [50], based on Jordaan and McKenna [42,43,51] and Jordaan et al. [27], are adopted as the foundation of the constitutive model presented herein. A progressive damage model with an iterative algorithm is proposed to address the issues regarding the unrealistically large stresses reported in [50,58]. The scalar limit of 26.0 MPa for the von Mises stress proposed by Turner [50] is replaced with a strain-rate and pressure-dependent failure function with an elliptical locus in $p - s$ space. Details are discussed in the following sections.

3. Numerical modelling of physical tests and preliminary results

Two different types of physical tests, indentation and creep, published in the literature are simulated in the present study to examine and validate the constitutive equations. Details of the physical tests and the corresponding numerical models developed herein are discussed in this section.

3.1. Creep tests

Xiao [12] carried out triaxial compressive creep tests on cylindrical ice samples, shown schemetically in Fig. 2a, to validate the constitutive equations outlined in the previous section. The cylindrical specimens were made of laboratory-prepared granular ice, following the procedure detailed in [59]. The granular ice was produced in a cylindrical, acrylic mould with a diameter of 229 mm and a height of 303 mm. After filling with 2.00–3.36 mm ice seeds, the mould was flooded with distilled, deionized, deaerated water, and the freezing process was conducted at –10°C. The products of the freezing process were then machined to cylinders with 70±0.05 mm in diameter and 175±1.0 mm in height. The triaxial compressive creep tests were conducted on both intact and pre-damaged specimens with a variety of axial loads and confining pressures. Three of these tests using intact specimens have been repeatedly employed in recent studies to validate the material models developed for simulating the viscoelastic behaviour of ice [58,60,61]. These three tests, also employed in the present study as a reference to validate the material model, include an intact ice specimen subject to a confining pressure of 10 MPa and an axial load that is different in each test (i.e., P_{cnf}=10 MPa and P_{ax}=5, 7, and 10 MPa in Fig. 2). The loads are applied with a rectangular pulse profile (red solid line in Fig. 1b) so that an instant load with a constant magnitude is applied for 20 s followed by an instant unload to zero lasting for 20 s to measure the strain recovery (Fig. 3). Note that the unloading phase was longer than 20 s in the physical tests [12], but only 20 s of which was simulated in [60] to diminish the computational costs (the unloading phase was not simulated in [58,61]). The total 40 s duration (20 s loading followed by 20 s unloading) is adequate for the model verification given that the duration of impact load in ice-structure collision events is much shorter than 40 s. In addition, the curves almost level out following 20 s of unloading.

To simulate the triaxial creep tests in the present study, an axisymmetric finite element model, shown in Fig. 2b was developed using Abaqus/CAE 2019 [28]. The material behaviour was modelled by the VUMAT demonstrated in Fig. 4 with the damage model DMa, termed hereafter 'VUMAT-DMa'. This VUMAT is written in FORTRAN based on

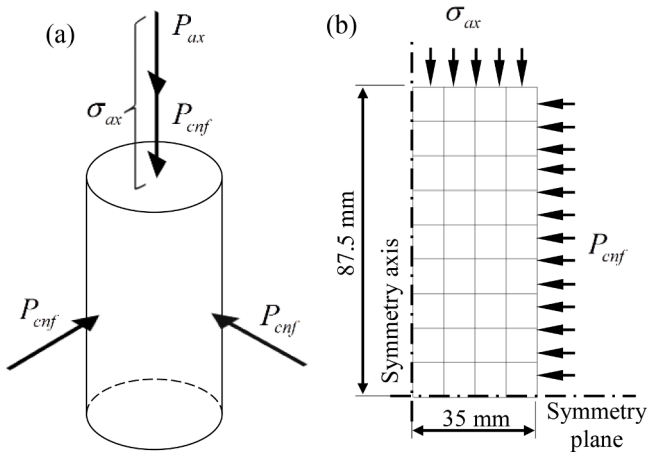

Fig. 2. (a) Illustration of the triaxial creep test specimen under confining pressure, P_{cnf}, and additional axial pressure, P_{ax}, which together cause the compressive axial stress, $\sigma_{ax} = P_{ax} + P_{cnf}$. (b) The axisymmetric finite element model of the triaxial creep test developed in the present study.

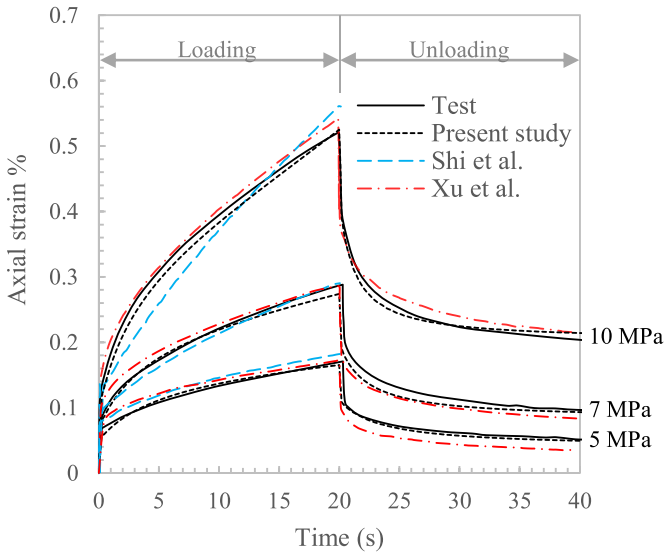

Fig. 3. Axial strain history for three axial loads (5 MPa, 7 MPa, and 10 MPa) from the physical tests [12], the viscoelastic VUMAT developed in the present study (DMa branch in Fig. 4), the viscoelastic model of Shi et al. [58], and the viscoelastic-plastic model of Xu et al. [60].

the constitutive equations proposed by Xiao [12] (i.e., Eqs. (6)–(24)). The axisymmetric domain in Fig. 2b is discretised into 36 linear quadrilateral elements with reduced integration (CAX4R). The model was found insensitive to element size mostly due to the small deformations and in part because of the axisymmetric load and geometry. The axial strain results produced by the finite element models using the material parameters listed in Table 1 are plotted in Fig. 3, which correlate very closely with the experimental strain histories. It is worth noting that 3D hexahedral finite element models of the creep tests were also developed, and they produced essentially the same results as the axisymmetric models. For concision and clarity, only the results of the axisymmetric models are plotted in Fig. 3

Despite modelling the same physical tests, different studies [12,58,60] have reported different material properties for the intact ice specimen. While the elastic modulus of intact ice (modelled with the spring stiffness in the Maxwell unit, E_M) was experimentally measured to be 9.5 GPa in the reference study [12], the values 11.8 GPa and 14.0 GPa were used for the elastic modulus, E_M, in [58] and [60], respectively (the elastic modulus 14.0 GPa is calculated from the shear and bulk moduli and Poisson's ratio provided in [60] as this reference has not disclosed the value of E_M). Given that the elastic modulus is a physical property found directly from the instantaneous response of the ice specimen, the 9.5 GPa measured experimentally in [12] is bound to be the most accurate value among the three reported values. Therefore, the elastic modulus of ice in the triaxial creep test simulations of the present study is set to 9.5 GPa. The elastic stiffness in the Kelvin unit, E_k, also varies significantly in the references noted above [12,58,60]. E_k in [58] and [60] is 8.36 GPa and 0.933 GPa, respectively (the value 0.933 GPa is calculated from the equations and the parameter values provided in [60] as the value of E_k is not reported in this reference). Xiao's calibration study in [12], however, yielded E_k= 9.5 GPa. That said, Xiao also used a different value, 3.8 GPa, for E_k in another study [11] to simulate the triaxial creep tests with ice samples prepared and tested under the same conditions. These inconsistencies might be because E_k is a phenomenological parameter and its value could depend on the value of other phenomenological parameters. A calibration analysis in the present study gave 5.0 GPa for E_k which is between the two values reported in [11] and [12]. The values of the other parameters are listed in Table 1.

3.2. Cone-shaped ice crushing tests

The VUMAT-DMa accurately modelled the triaxial creep tests in the previous section. The capability of this VUMAT in modelling the progressive crushing of ice, typical in ice-structure collision events, is investigated in this section. Two ice crushing tests with flat rigid indenters, carried out by Kim et al. [29] with the experimental set-up displayed in Fig. 5a, are simulated. The only difference between the two tests is the indentation speed, V, set to 100 mm/s for the first test and 1 mm/s in the second one. The first test better represents the loading rates in collision scenarios. However, to ensure the material model can correctly capture the strain rate (loading rate) effects, the second test is also simulated.

For computational efficiency, a quarter finite element model, shown in Fig. 5, was developed to simulate the physical tests (the geometry and load were assumed to remain generally symmetrical during the simulation). A preliminary study with both a quarter model and a full model was carried out to ensure that the full and the quarter model produce very similar results. The ice domain was discretised with ~3 × 3 × 3 mm^3 reduced integration hexahedral elements (C3D8R), found through a mesh sensitivity analysis to produce mesh-independent results. The uniform mesh in Fig. 5 was produced via a manual, incremental meshing process, known as 'bottom-up meshing', since an automatically generated mesh for the conical geometry would include elements with significantly different sizes, shapes and aspect ratios. These elements, generated by automatic meshing, could have poor quality leading to smaller time increments and more expensive computations or even premature excessive element distortions that cause simulation failures. The uniform mesh generated using the bottom-up technique, however, comes with the disadvantage of having an uneven surface at the base of the model (i.e., the bottom surface of the model). This uneven surface is not expected to affect the numerical results as the maximum indenter displacement, D, in the simulations is 26 mm which provides a significant distance between the base and the indentation stop point (Fig. 5b).

To simulate the constraints induced by the ice holder, an extra layer of elements has been developed at the base, and all the element nodes located outside of the target ice domain are fixed (i.e., all nodes inside the dashed box in Fig. 5b). Besides, all the nodes located on the cylindrical side of the model except for the ones on the edge connecting the cylindrical section to the conical section are only allowed to move along the vertical direction (i.e., X direction) to simulate the effect of the vertical surface of ice holder. These boundary conditions provide very similar constraints to those in the physical tests. In the physical tests [29], the indenter had two stop-start points (D≈9 mm and D≈179 mm) for data collection purposes that caused two large drops/discontinuities in the F-D curves (see the experimental curves in Figs. 6, 7, and 8). To simulate the effect of these stop-start points on the numerical F-D curves, the indenter displacement is paused at D≈9 mm and D≈179 mm for 0.5 ms in the 100 mm/s test and 500 ms in the 1mm/s test. These settings have provided good agreements between the numerical and experimental results discussed in Section 5.

The viscoelastic model discussed in Section 2 is supposed to simulate the softening in crushing ice until the crushed/pulverised substance is extruded out of the interaction interface. Therefore, ideally, the finite elements should not be eroded/deleted from the analysis. However, keeping the excessively distorted elements in the analysis cause simulation failure. In a preliminary study with the mesh configuration shown in Fig. 5, it was found that the simulations fail with an excessive distortion error message when the equivalent strain, ε, is between 1.0 and 1.5. Therefore, an element erosion criterion is set in this study that activates the erosion when ε exceeds 1.0. The effect of element erosion on the reaction force would be negligible if the eroding element with ε=1.0 contains a significantly softened substance with a remaining strength negligible compared to intact ice. To investigate this hypothesis, two different numerical modelling methods, ALE-FEM and coupled FEM-SPH, are employed that could minimize the artificial strength loss

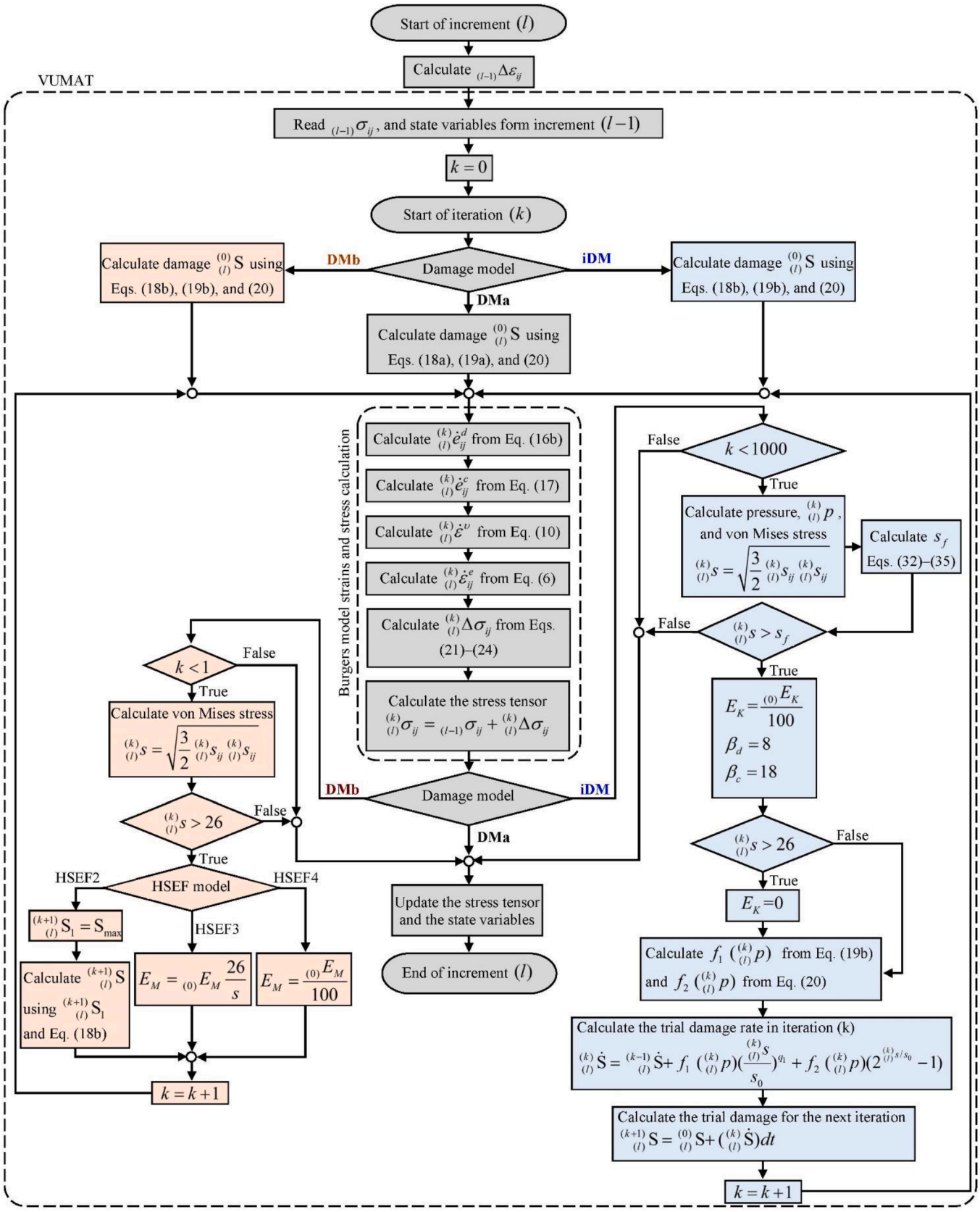

Fig. 4. The viscoelastic VUMAT with three different damage models, DMa, DMb, and iDM given in three branches.

Table 1
The model parameters used to simulate the triaxial creep test simulations.

Parameter	Value	Reference
E_M (GPa)	9.5	[11,12,48,49,58]
E_k (GPa)	5.0 (9.5)	Calibration[a] ([12])
ν	0.3	[11,12,48,49]
$\dot{\varepsilon}_0^d$ (s^{-1})	1.0×10^{-5}	[11,12,48,49]
$\dot{\varepsilon}_0^c$ (s^{-1})	1.76×10^{-7}	[11,12,48,49]
n	1.9	Calibration [b]
m	2.5	[12,48]
f_3	0.11	[11,12,48]
s_0 (MPa)	15.0	[12,48,49,58]
q_1	2.4	[48,58]
a_1 (s^{-1})	0.712	[12,49]
a_2 (s^{-1})	0.1	[12,49,50]
p_1 (MPa)	37.0	[12,49]
p_2 (MPa)	42.8	[12,49,50]
r	5.0	[12,49,50]
β_d	1.0 (8.0)	[12,48,49] ([62]) [c]
β_c	1.0 (18.0)	[12,48,49] ([62]) [c]

[a] The value of E_k is reported to be 9.5 GPa in [12] and 3.8 GPa in [11]. 5.0 GPa, found in the present study to produce the best fit with the physical creep test results (shown in Fig. 3), is between these two values. However, both 5.0 and 9.5 GPa are used in, a sensitivity analysis for cone-shaped ice crushing simulations in Section 3.2.

[b] n=2.0 was reported in [49] which is slightly higher than the 1.9 found in the present study from a calibration analysis.

[c] The set, 1.0 and 1.0 for β_d and β_c is used for the triaxial creep test simulations. However, an additional set of values for β_d and β_c, 8.0 and 18.0 reported in [62], is used in a sensitivity analysis for cone-shaped ice crushing simulations in Section 3.2. In iDM damage model, β_d and β_c are material state dependent parameters with the initial values of 1.0 and 1.0 which change to 8.0 and 18.0 upon the intuition of the HSEF phase (see Section 4 for more details).

due to the element erosion [28]. These methods can significantly increase computational costs and should be used when necessary.

Arbitrary Lagrangian-Eulerian (ALE) adaptive meshing allows for maintaining a high-quality mesh when large deformations or loss of material occur. This is because ALE adaptive meshing combines the features of pure Lagrangian and pure Eulerian analyses allowing the mesh to move independently of the material so that the mesh topology (elements and connectivity) is maintained under extreme deformations [28].

Coupled FEM-SPH method takes advantage of the intrinsic strength of both Lagrangian FEM and Smoothed Particle Hydrodynamics (SPH) method by converting Lagrangian elements to SPH particles when the conversion criterion is met. This method overcomes the numerical issues caused by the conventional element erosion technique such as the artificial loss of strength in the material and the loss of contact at the interaction interface because the generated particles can withstand deformations beyond the finite element distortion limits [28]. The conversion criterion in this study is the same as the erosion criterion, ε=1.0. Therefore, the difference between the reaction force histories produced by the Lagrangian FEM and the coupled FEM-SPH method could imply how much of the material strength is lost artificially due to the element erosion. The model is set to generate one particle per parent element at the beginning of the analysis. The particles remain inactive until the conversion criterion is met, upon which the parent element is removed from the analysis and the particle becomes active.

For ease of identification, the numerical models developed and discussed in this section are labelled according to their numerical modelling method, damage model, parameter values (E_k, β_d and β_c), and indentation speed (Table 2). The first numerical model, FEM-DMa-5.0-1-1-V100, has the same damage model (DMa) and parameter values (Table 1) as the numerical model validated in the previous section against the triaxial creep tests. The reaction force, F, produced by this model for the 100 mm/s crushing test, plotted in Fig. 6a, is extremely higher than the experimental reaction force. This overestimation was expected considering that the viscoelastic material model with DMa, VUMAT-DMa, is reported to produce unrealistically large stresses for high strain rates [58] or when the high-shear elastic failure occurs in ice [50] (see Section 2 for details).

In an effort to achieve better agreement with the experimental results, the simulation has been repeated using FEM-DMa-5.0-8-18-V100 which has the same numerical specifications as the first model except for the values assigned to the creep enhancement factors (i.e., β_d= 8 and β_c=18). These higher values for the creep enhancement factors were reported in [62] for simulating only one crushing cycle in an ice indentation test (see [62] for more details about a crushing cycle). The larger β_d and β_c have improved the numerical results in Fig. 6a, but not enough to achieve a good correlation with the experimental data. Therefore, the trial simulations are continued with a new group of three numerical models, Group 2, in which the damage model and high-shear elastic failure models proposed by Turner [50] are implemented instead of the damage model DMa.

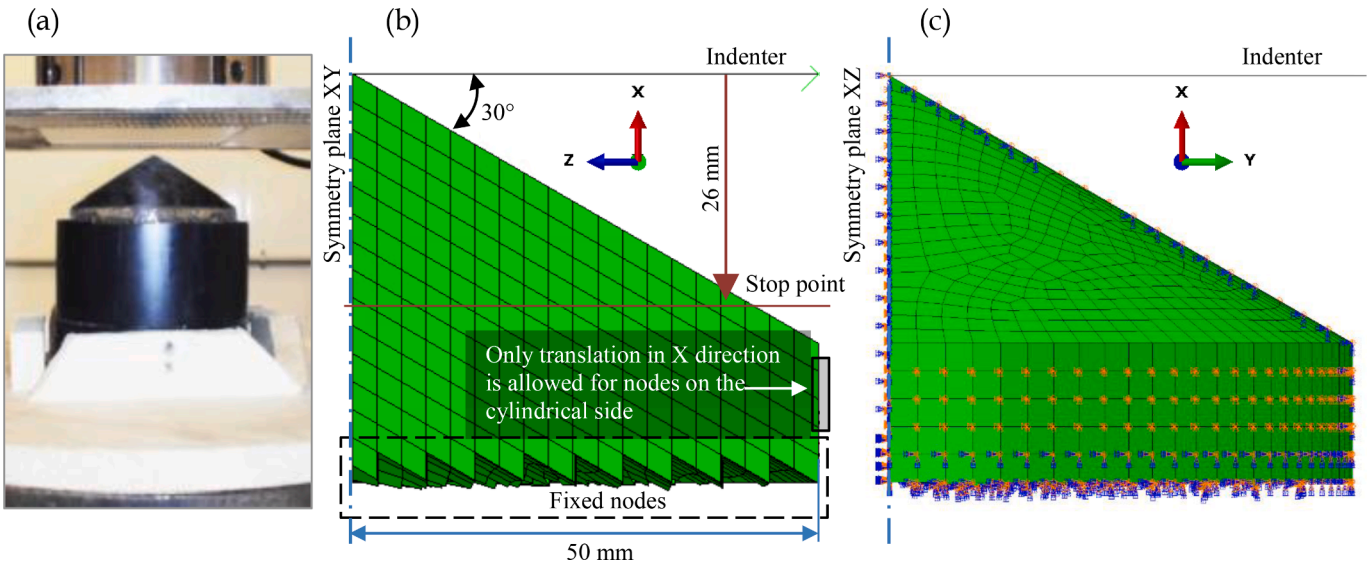

Fig. 5. (a) Experimental set-up [29]. (b) Front view of the finite element model with 3 mm elements in a uniform mesh. (c) Back view of the finite element model with boundary condition symbols displayed.

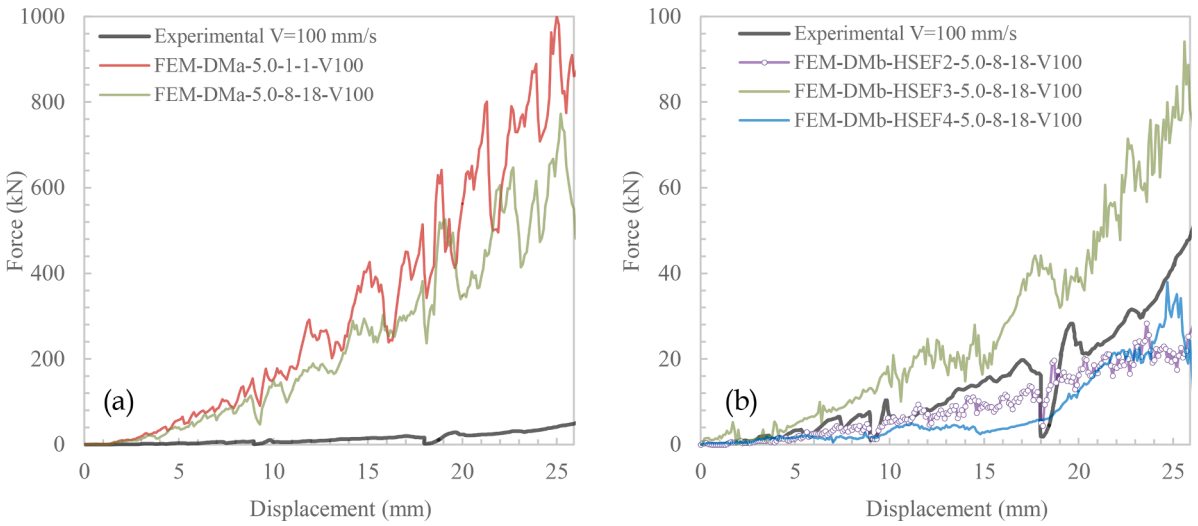

Fig. 6. Force vs. displacement investigated for the effects of (a) creep enhancement factors, (b) the damage model and high-shear elastic failure model.

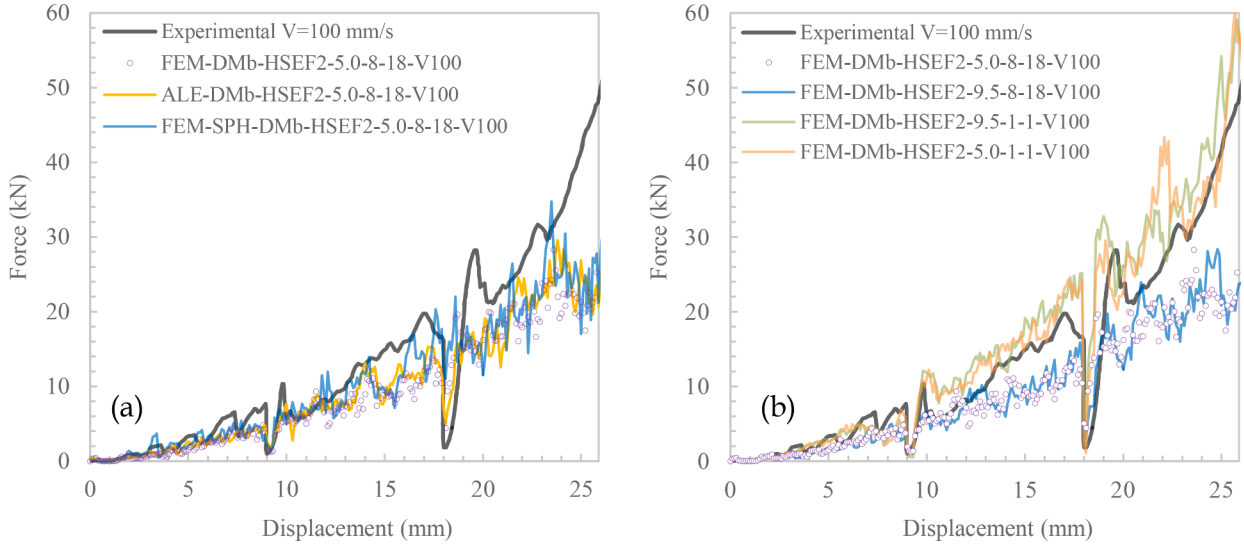

Fig. 7. Force vs. displacement investigated for the effects of (a) numerical modelling method and (b) the uncertain parameters,E_k, β_d and β_c.

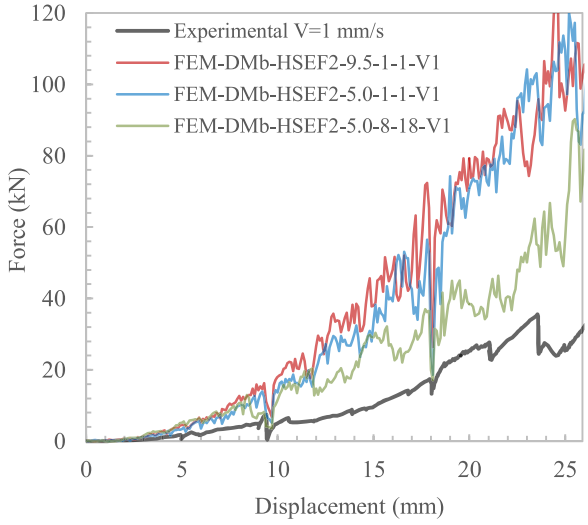

Fig. 8. Force vs. displacement investigated for the effect of loading rate.

The modifications suggested by Turners have significantly improved the numerical results. Among the three new models, the model with HSEF2 has returned the best correlation with the experimental data. This model, however, has slightly underestimated the reaction force (compare the numerical and experimental curves in Fig. 6b). Whether this underestimation is caused by element erosion is investigated by changing the numerical method from Lagrangian FEM to ALE-FEM and coupled FEM-SPH. Figure 7a shows that the effect of the numerical modelling method on the *F-D* curves is not noticeable. This is due to the large damage index (S_1=14.0) used in HSEF2 which has caused significant softening in the elements so that they do not produce any significant reaction force after ε=1.0 (the erosion criterion). Therefore, converting them to SPH particles at ε=1.0 has just slightly increased the total reaction force, and the results of the ALE method are essentially the same as the Lagrangian FEM.

Another possible reason for the underestimation of the reaction force by FEM-DMb-HSEF2-5.0-8-18-V100 could be the uncertainties associated with some of the parameters in the literature. As discussed earlier there are greatly different values reported for E_k, β_d and β_c (addressed as uncertain parameters in Table 2) by the authors of the viscoelastic model for ice crushing simulations. In order to address the underestimation of

Table. 2
Details of the numerical models discussed in Section 3.

Group No.	Model #	Numerical method	Damage model	HSEF model	Uncertain parameters E_k (GPa)	β_d	β_c	Indentation speed, V (mm/s)
1	FEM-DMa-5.0-1-1-V100	Lagrangian FEM	DM-a	N/A	5.0	1	1	100
	FEM-DMa-5.0-8-18-V100	Lagrangian FEM	DM-a	N/A	5.0	8	18	100
2	FEM-DMb-HSEF2-5.0-8-18-V100	Lagrangian FEM	DM-b	HSEF2	5.0	8	18	100
	FEM-DMb-HSEF3-5.0-8-18-V100	Lagrangian FEM	DM-b	HSEF3	5.0	8	18	100
	FEM-DMb-HSEF4-5.0-8-18-V100	Lagrangian FEM	DM-b	HSEF4	5.0	8	18	100
3	ALE-DMb-HSEF2-5.0-8-18-V100	ALE-FEM	DM-b	HSEF2	5.0	8	18	100
	FEM-SPH-DMb-HSEF2-5.0-8-18-V100	FEM-SPH	DM-b	HSEF2	5.0	8	18	100
4	FEM-DMb-HSEF2-9.5-8-18-V100	Lagrangian FEM	DM-b	HSEF2	9.5	8	18	100
	FEM-DMb-HSEF2-9.5-1-1-V100	Lagrangian FEM	DM-b	HSEF2	9.5	1	1	100
	FEM-DMb-HSEF2-5.0-1-1-V100	Lagrangian FEM	DM-b	HSEF2	5.0	1	1	100
5	FEM-DMb-HSEF2-9.5-1-1-V1	Lagrangian FEM	DM-b	HSEF2	9.5	1	1	1
	FEM-DMb-HSEF2-5.0-1-1-V1	Lagrangian FEM	DM-b	HSEF2	5.0	1	1	1

reaction force by FEM-DMb-HSEF2-5.0-8-18-V100, another group of three models (Group 4 in Table 2) with the same settings as FEM-DMb-HSEF2-5.0-8-18-V100 but with different values for E_k, β_d and β_c are developed. To increase the reaction force, in the first model of Group 4, E_k is set to 9.5 GPa as per [12]. This change did not make a noticeable difference in the *F-D* results (Fig. 7b). Hence, in the second model of Group 4, in addition to having E_k set to 9.5 GPa, β_d and β_c are dropped to their original values given in Table 1 (i.e., β_d=β_c=1.0) to decrease the creep strain and increase the material strength. With these changes, the reaction force has increased so that the numerical *F-D* curve sits only slightly higher than the experimental one (Fig. 7b). In the last attempt in Group 5, the original values of β_d and β_c are kept (i.e., β_d=β_c=1.0) and E_k is set back to its original value in Table 1 (i.e, E_k=5.0) to reduce the slight overestimation of the reaction force. Figure 7b demonstrates a slight reduction in F when E_k is dropped from 9.5 to 5.0 GPa but the diminution is too small to make any noticeable difference in the *F-D* curve. Consequently, the numerical *F-D* curve is still higher than the experimental one, but the difference is acceptable. Hence, the numerical study is continued with the settings applied in FEM-DMb-HSEF2-9.5-1-1-V100 and FEM-DMb-HSEF2-5.0-1-1-V100, both of which provided acceptable agreements with the 100 mm/s physical test. The indentation speed in these two models was changed to 1 mm/s to create the models in Group 5 (Table 2) for simulating the 1 mm/s physical crushing test.

Fig. 8 shows that the numerical models that provided a good agreement with the experimental results for the 100 mm/s indentation speed have largely overestimated the reaction force in the 1 mm/s case. Furthermore, having Fig. 8 compared with Fig. 7b, the reaction force is increased by dropping the indentation speed which contradicts the experimental results in [29]. The reason lies in the high-shear elastic failure model, which unlike the viscoelastic stress-strain relations is not rate-dependent. Using the viscoelastic model, a certain stress intensity (e.g., 26 MPa) can be produced in an element in two different ways, small deformation with a high strain rate or large deformation with a

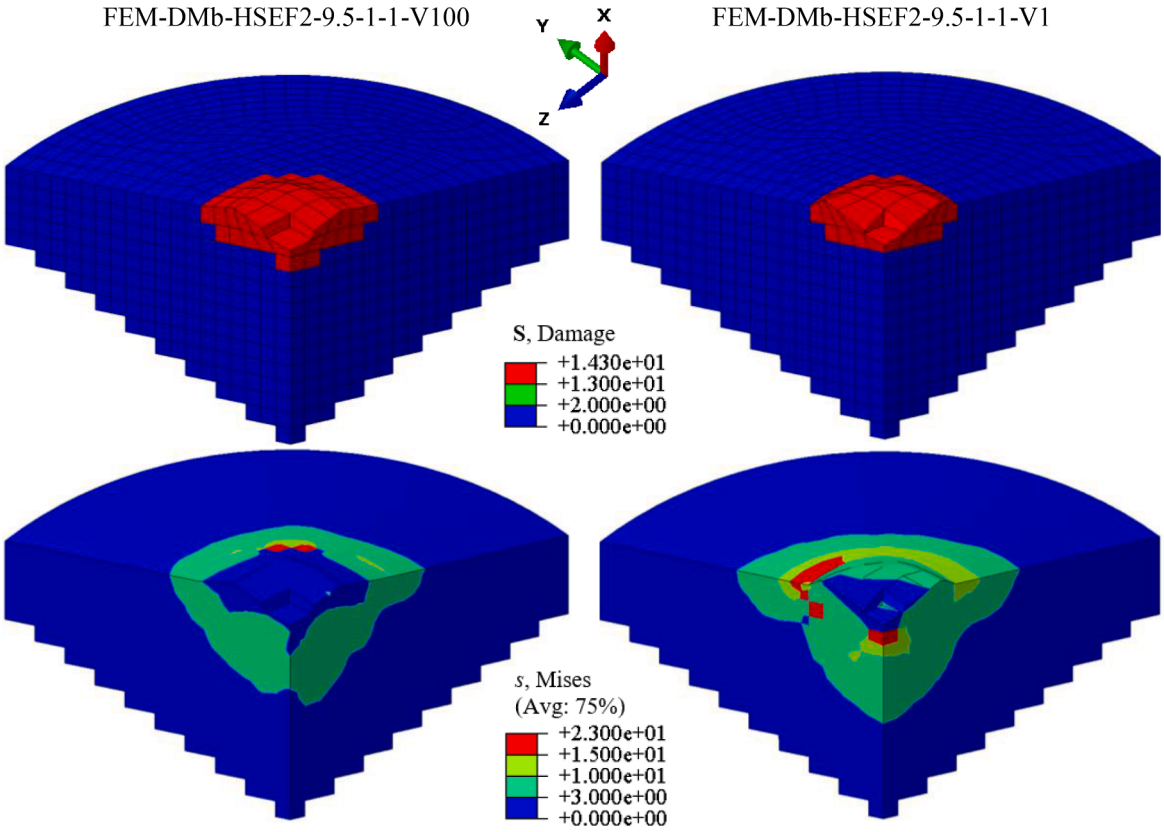

Fig. 9. The effect of loading rate on the HSEF zone (top row) and stress (bottom row) when HSEF2 model is implemented.

low strain rate. It means that the elements in the 100 mm/s test exceed the HSEF threshold (26 MPa) earlier and with less deformation/strain compared to the elements in the 1 mm/s case. As mentioned earlier, HSEF2 enforces a value of 14.0 on S_1 once the von Mises stress in an element surpasses 26.0 MPa, which causes an abrupt marked escalation in the damage index, S, (from below 2.0 in blue elements to above 14.0 in red elements in Fig. 9). This significantly softens the material in the HSEF zone so that the stress in this zone drops far below 26.0 MPa (Fig. 9). Therefore, elements have a significantly higher energy dissipation rate before undergoing HSEF, meaning that the longer they last before experiencing HSEF, the more energy they absorb. Therefore, the elements in the 1 mm/s case absorb more energy compared to the 100 mm/s case as they need larger deformations to exceed 26 MPa (the HSEF criterion). Additionally, the HSEF zone (red elements in the top row of Fig. 9) in the 100 mm/s test is larger than the 1 mm/s one due to the same mechanism just described. A larger HSEF zone means a larger region of low stress with less resistance against the indenter displacements.

To address the shortcomings of HSEF2 in capturing the strain rate effect, a rate dependent HSEF model with a systematic method for determining the value of the damage index beyond the HSEF threshold instead of applying an arbitrary flat value is required. An HSEF model with such qualities embedded in a damage model with an iterative algorithm is proposed in the following section.

4. Pressure- and rate-dependent damage model with an iterative algorithm

It is well established that the ultimate/yield/failure strength of ice is a pressure- and rate-dependent property [63–76]. Having analysed the experimental results from around 300 physical triaxial tests covering a wide range of strain rates ($10^{-6}<\dot{\varepsilon}<10^{-1}$ s^{-1}) and hydrostatic pressures ($0.1<p<85.0$ MPa), Derradji-Aouat [72] demonstrated that the failure stress data plotted in p-τ_{oct} space ($\tau_{oct}=\sqrt{\frac{s_{ij}s_{ij}}{3}}$is the octahedral shear stress) follow an elliptical curve expressed by

$$\left(\frac{\tau_{oct}-\eta}{\tau_{\max}}\right)^2+\left(\frac{p-\xi}{p_c}\right)^2=1 \tag{31}$$

where η, $\tau_{\max}$, ξ, and p_c are constants ($\eta=0$). In the present study, Eq. (31) is rewritten in the p-s space as

$$\Phi\equiv\varphi(p,s)=\sqrt{s^2+\alpha^2(p-p_0)^2}-B=0 \tag{32}$$

where $\Phi\equiv\varphi(p,s)$ is the failure strength function;$B=\alpha A=\alpha\left(\frac{p_c+p_t}{2}\right)$ is the vertical semiaxis of the ellipse (along the s-axis in Fig. 10b); $\alpha=\frac{B}{A}$ is the shape factor of the elliptical failure envelope that determines the relative magnitude of the semiaxes; A is the horizontal semiaxis of the elliptical failure envelope (along the p-axis); $p_0=\frac{p_c-p_t}{2}$ is the centre of the ellipse on the p-axis, and p_t and p_c denote the ice material strength under hydrostatic tension and hydrostatic compression, respectively (p_c should be always positive). To obtain the shape factor,α, failure stress in

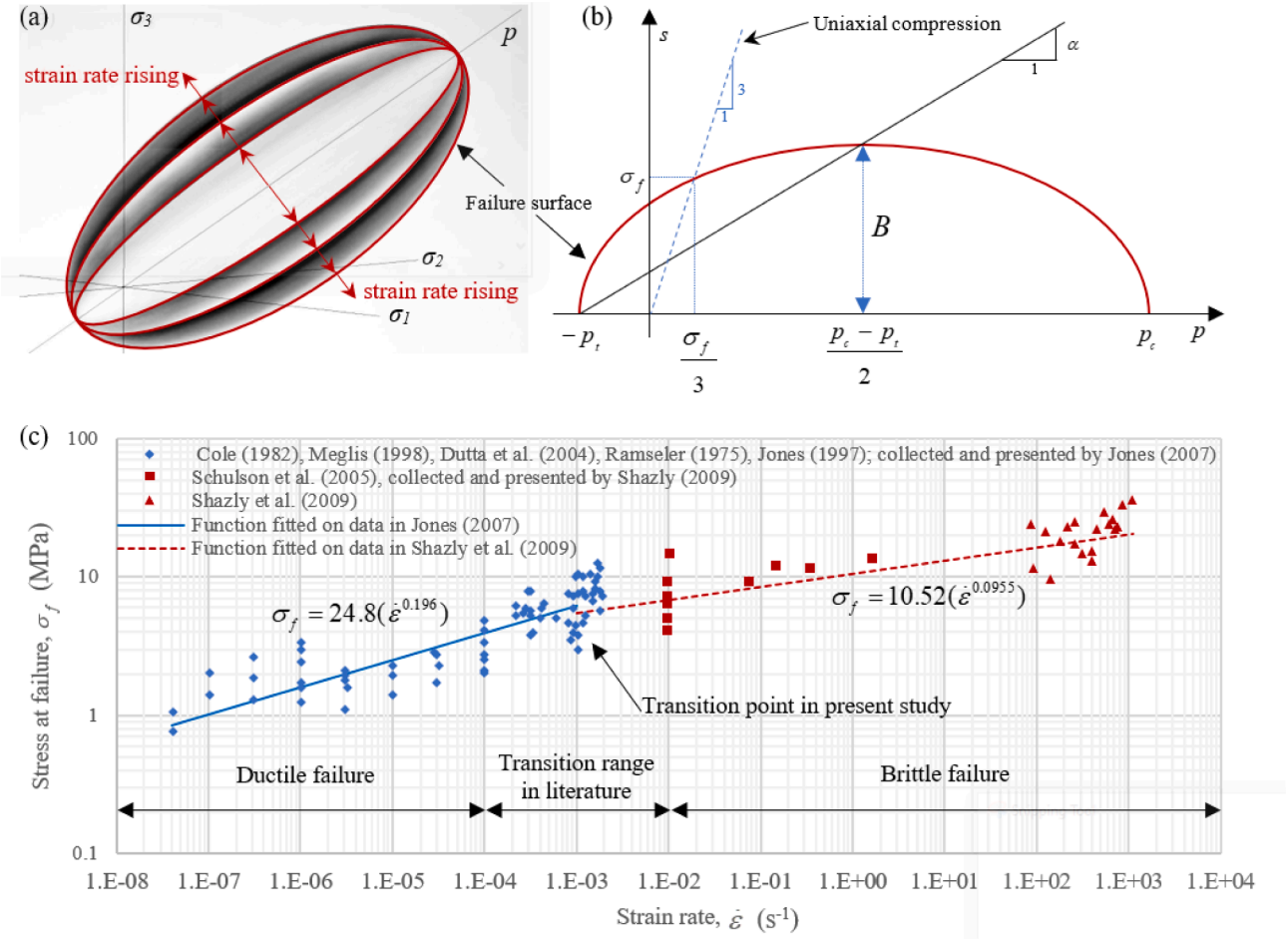

Fig. 10. The failure loci of freshwater polycrystalline ice material; (a) evolution in principal stress space ($\sigma_1-\sigma_2-\sigma_3$); (b) the elliptical envelope in the p-s space; (c) strain rate dependency graph in terms of uniaxial compressive strength (recreated using the data presented in [1,20]).

uniaxial compression test, σ_f, failure strength in hydrostatic compression, p_c, and the failure strength in hydrostatic tension, p_t, are required and calculated by

$$\alpha = \frac{3k}{\sqrt{(3k_t + k)(3 - k)}}; k = \frac{\sigma_f}{p_c}; \; k_t = \frac{p_t}{p_c} \tag{33}$$

To have a valid failure surface, the strength ratios must meet

$$0 < k < 3 \text{ and } k_t \geq 0 \tag{34}$$

Derradji-Aouat [72-74,76] showed that for any given strain rate, p_t and p_c remain almost unchanged while B increases with the strain rate. This creates a set of concentric elliptical failure loci (Fig. 10a). The strain rate hardening of ice is known to be disrupted at a certain range of strain rates, termed 'ductile-to-brittle transition' strain rate, which is reported to be between 10^{-4} and 10^{-2} s^{-1} in various studies [17–25]. During the transition stage, ice strength remains constant or decreases slightly and then continues to rise with the strain rate in the brittle regime, but with a slower rate compared to the ductile regime (Fig. 10c). To capture this phenomenon in the present study the relation between ice strength and strain rate developed by Jones [20] for iceberg ice is employed for the ductile regime ($\dot{\varepsilon} \leq 0.001$ in Eq. (35)). For the brittle regime, the relation developed by Shazly et al. [1] obtained from a series of high strain-rate compression tests on single crystal and polycrystalline ice using split Hopkinson pressure bar (SHPB) is adopted ($\dot{\varepsilon} > 0.001$ in Eq. (35)). The reason for choosing Shazly et al. study is that their equation is obtained from a much broader range of strain rates in the brittle regime, from 10^{-2} to 1000 s^{-1}. This was made possible by the SHPB technique which also provides better accuracy in material strength measurements at high strain rates as opposed to the quasi-static testing techniques which can cause considerably scattered results and uncertainties.

$$\sigma_f = \begin{cases} 24.8\left(\dot{\varepsilon}^{0.196}\right) & \text{if} \quad \dot{\varepsilon} \leq 0.001 \\ 10.52\left(\dot{\varepsilon}^{0.0955}\right) & \text{if} \quad \dot{\varepsilon} > 0.001 \end{cases} \tag{35}$$

Having σ_f obtained form Eq. (35), the pressure and strain-rate dependent failure stress, s_f, can be found from Eq. (32). In the present study, the high-shear elastic failure introduced in [50] is set to occur when the von Mises stress exceeds the failure stress, $s > s_f$. The experimental observations reported by Turner [50] showed that the failure strength is not fixed at 26.0 MPa, but it reduces as the confining pressure increases from mid-to-high levels. This behaviour is in line with the theory of the elliptical failure surface. As per the discussion provided in the previous section, the damage index should increase significantly in the HSEF phase; however, it is not clear to what extent. Hence, a new damage model, termed 'iDM', with the iterative algorithm given in Fig. 4 (see iDM branch), is proposed to iteratively correct the value of the damage parameter, S, in the HSEF phase. The damage model iDM incorporates two failure phases. In the first phase, $s_f < s \leq 26.0$, the Kelvin spring stiffness, E_K, is dropped to $\frac{E_K}{100}$, (instead of E_M in HSEF4), which is inspired by the work of Meaney et al. [62] who also suggested the two large constant values for β_d and β_c (i.e., 8 and 18) for damaging ice and the highly-crushed layer. The maximum allowable value of B in the damage model is set to 26.0 MPa, meaning that the vertical semiaxis of the failure envelope grows with the strain-rate per Eq. (35), as long as $B > 26.0$ MPa, beyond which the failure envelope size remains unchanged. In the second failure phase, $s > 26.0$ MPa, E_K is reduced to zero, eliminating the delayed elastic response in the highly-crushed extruding layer under high stresses. The iterations in iDM continue until $s \leq s_f$ or $k \geq 1000$, where k is the loop counter.

It should be noted that, unlike HSEF2 which was used as a guide to develop iDM, the increase in the damage index in iDM is applied directly to the total damage index, S, not through increasing the microcracking damage index, S_1. This is because, the microcracking damage in ice under high pressures becomes almost zero (Eq. (19b)), and consequently S_2 controls the damage intensity. Therefore, the damage value correction was applied directly to S so that in all pressure levels (low, medium and high) the stresses beyond the failure surface could be returned to the surface by increasing the damage index.

5. Results and validation of the iterative damage model iDM

Having iDM implemented in the VUMAT, the 100 mm/s crushing test is simulated with Lagrangian FEM, ALE-FEM, and coupled FEM-SPH methods. The numerical *F-D* results plotted against the experimental data in Fig. 11 show that the Lagrangian FEM has underestimated the reaction force. However, the numerical results produced using ALE-FEM and the coupled FEM-SPH methods are closely correlated with the experimental data. This means that the reaction force underestimation made by the Lagrangian FEM in this section is caused by the element erosion. Unlike most plasticity models, the viscoelastic model appears to have simulated the physical force oscillation typical to the ice indentation tests even before the element erosion occurs. The force oscillation in physical ice crushing tests is usually controlled by two major mechanisms, spalling and extrusion of the crushed layer. Given that spalling occurs only to a limited extent in the cone-ice crushing tests, the oscillation is mainly controlled by the extrusion. In most plasticity models, the oscillation is simulated artificially by the element erosion. Element erosion in the present study has also caused force drops that are responsible for the large oscillations seen in Fig. 11. The force oscillations observed before the first element erosion in Figs. 11 and 12 are simulated by the material model and are not artificial. In addition to the oscillations simulated by the material model or caused by element erosion, there is also noise in the numerical *F-D* curves typical in explicit simulations [28]. The noise filtered numerical results using the Butterworth filter with cutoff frequencies of 150 Hz and 1.5 Hz for the 100 mm/s and 1 mm/s tests, respectively, are also plotted in Figs. 11 and 12 (for details about the Butterworth filter refer to the Abaqus user's manual [28]).

To investigate the accuracy of the material model in capturing the strain rate effect, the 1 mm/s test is simulated with the ALE-FEM and coupled FEM-SPH methods which both produced good agreement with the experimental results (Fig. 12). The ALE-FEM method appears to have slightly better performance than the coupled FEM-SPH method at the beginning stage of the crushing test. However, in general, the coupled FEM-SPH method has a better performance than the ALE-FEM method as the ALE-FEM method has underestimated the reaction force of the 1 mm/s test at large indenter displacements, above 16 mm. Then again, the coupled FEM-SPH method needs significantly higher computational efforts as opposed to the ALE-FEM method (Table 3). Therefore, ALE-FEM method is recommended where computational efficiency is a priority. That said, the FEM-SPH method allows for keeping the excessively deformed material in the analysis. For example, Fig. 13 shows the capability of the viscoelastic material model with iDM damage in simulating the progressive extrusion of highly-crushed and pulverised ice throughout the crushing process when implemented with the coupled FEM-SPH method. This could be important in practical simulations where the initial impact could make a large dent in the structure confining the ice being crushed and pulverised. The extrusion of the pulverised ice under confining pressure then would change the force profile given that it should travel a long way under pressure before it is extruded away from the interaction interface. This proposition needs to be further investigated and confirmed in future studies.

Additionally, it is recommended to examine the scalability of the proposed constitutive laws and numerical methods from small-scale laboratory tests presented in this study to full-scale ice-structure collision events. For this purpose, the user must provide the input values for the parameters listed in Table 1, which may require recalibration for larger scale models. The failure surface incorporated in iDM can be adjusted if necessary by recalibrating p_b, p_c, and σ_f (Eq. (35)).

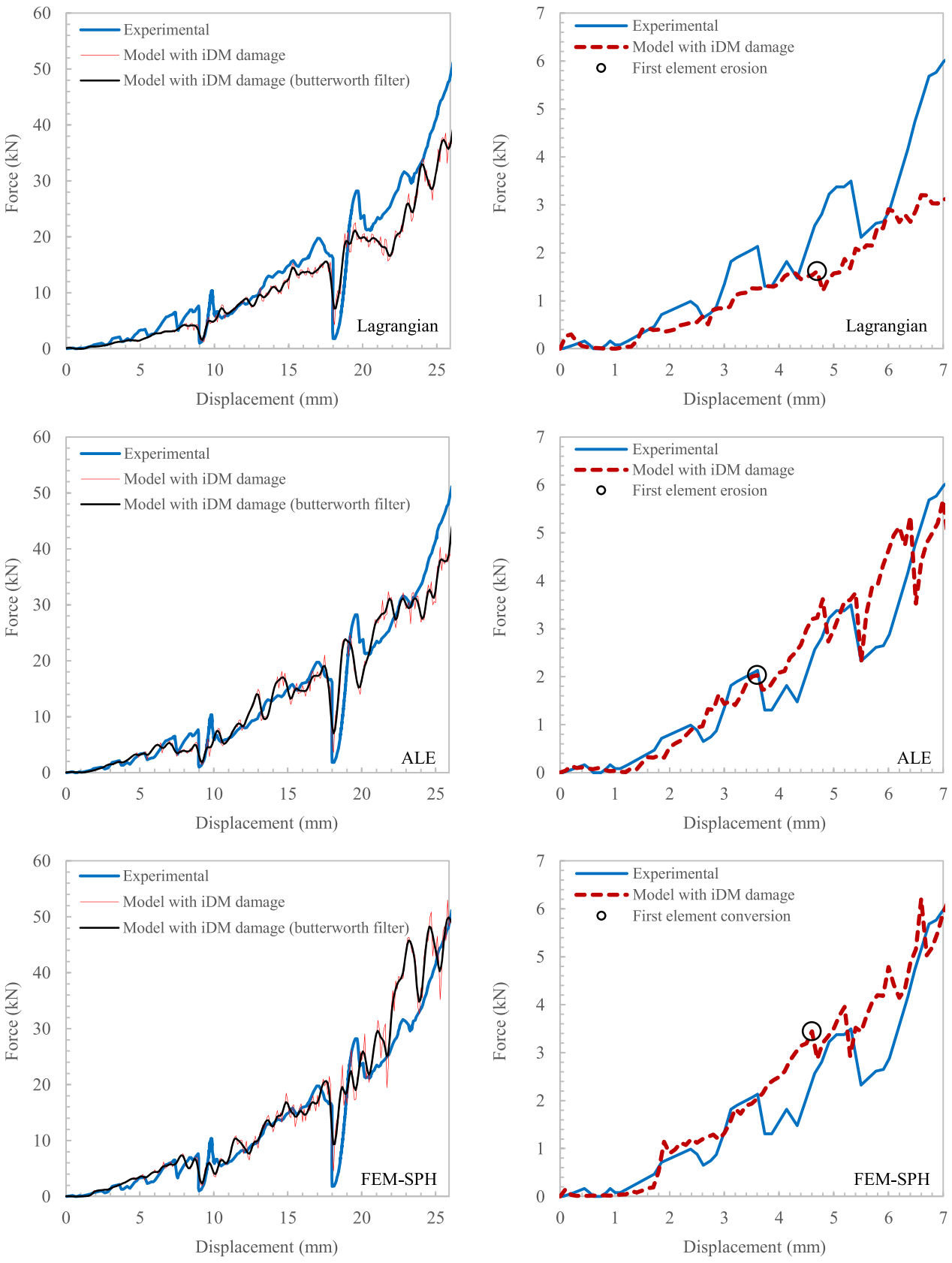

Fig. 11. Force vs. displacement obtained from the physical crushing test with V=100 mm/s and the simulation with iDM damage model and three different numerical methods (plots on the right side are magnifications of the first 7 mm of the plots on the left side).

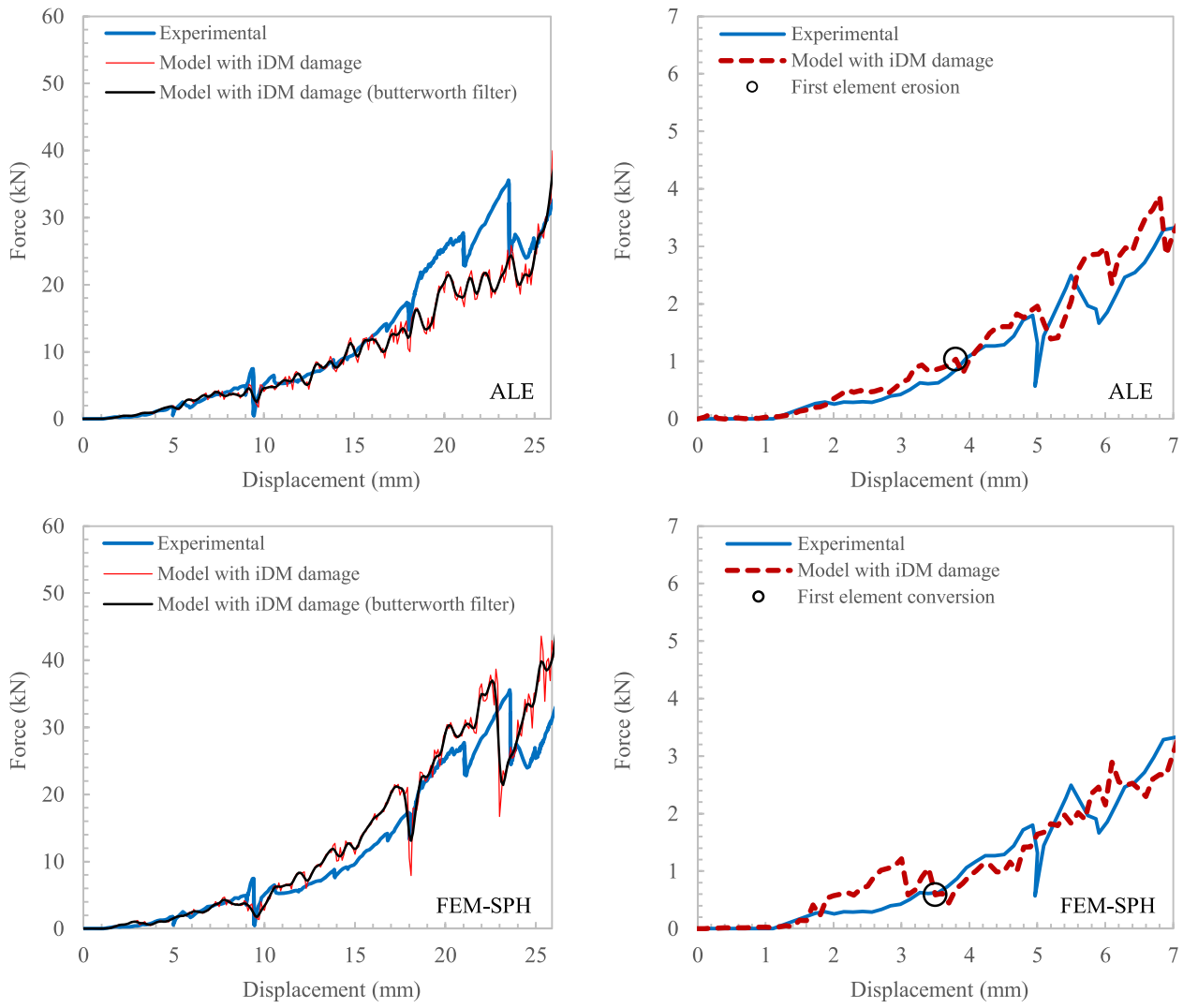

Fig. 12. Force vs. displacement obtained from the physical crushing test for V=1 mm/s and the simulation with iDM damage model and two different numerical methods (plots on the right side are magnifications of the first 7 mm of the plots on the left side).

Table 3
Executable time summary for the studied models using Intel(R) Xeon(R) CPU E5-2680 v3 2.50GHz with 12 cores.

Indentation speed (mm/s)	Numerical method	CPU time (s)
100.0	Lagrangian FEM	508
	ALE-FEM	1876
	FEM-SPH	2770
1.0	ALE-FEM	56068
	FEM-SPH	196227

6. Conclusions

The progressive crushing, pulverisation, and viscous extrusion of laboratory-scale polycrystalline ice were simulated using a nonlinear viscoelastic material model and a novel progressive damage model with an iterative algorithm. The nonlinear viscoelastic material model, written in Fortran VUMAT for Abaqus, was validated against physical triaxial compressive creep tests. The progressive damage model with the iterative algorithm, developed for glacial/freshwater polycrystalline ice colliding with marine structures, where the ice experiences high stress and exhibits high shear elastic failure in addition to microcracking, dynamic recrystallisation, and pressure melting, was validated against physical cone-shaped ice crushing tests with 1 mm/s and 100 mm/s indentation speeds. The results demonstrated that the material model with the proposed damage model correctly captured the strain rate effects. However, further validation of the proposed models may be required for other crushing speeds, particularly those outside the investigated range.

The simulations were carried out with three different numerical methods, Lagrangian FEM, ALE-FEM, and coupled FEM-SPH. The latter method in conjunction with the proposed damage model allowed for the simulation of phase transition from solid-like to fluid-like pulverised/granular ice.

A good correlation between the numerical and experimental force-displacement data was achieved with both ALE-FEM and coupled FEM-SPH methods. The ALE-FEM method had a slightly better agreement with the test results at the beginning of the indentation. However, in general, the results from the coupled FEM-SPH method correlated more closely with the experimental data because it could simulate extremely large deformations of pulverised ice during the extrusion phase by converting excessively distorted elements to SPH particles. This is important in practical applications where the initial impact might create a dent in the structure which could confine the crushed and pulverised ice during the rest of the interaction. Subsequently, the confined pulverised ice should travel a long way under high pressure before being extruded away from the interaction interface, which in turn is believed to significantly affect the reaction force profile. Further

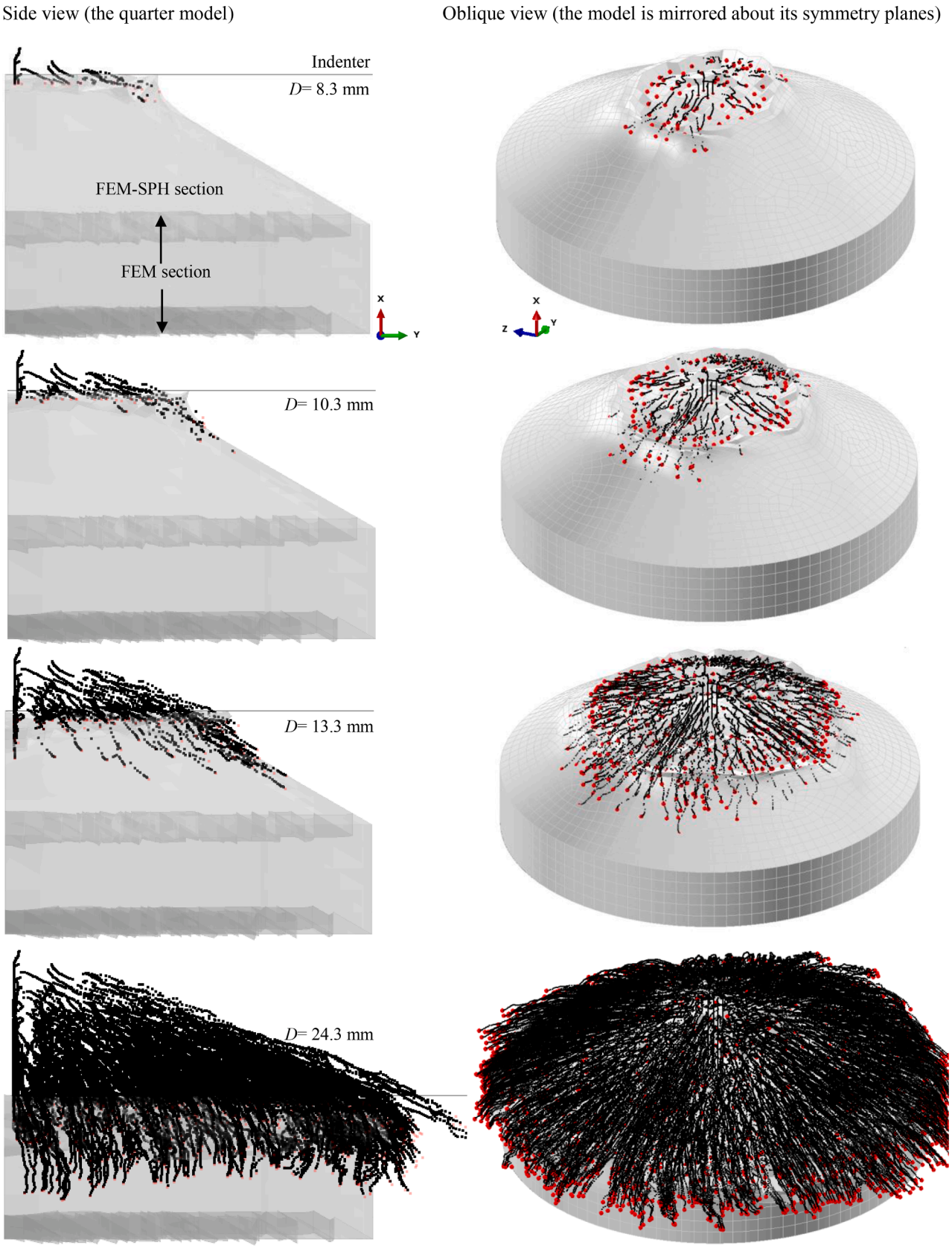

Fig. 13. Progressive extrusion of crushed ice simulated with SPH particles (red points) with tracing visualized (black dotted lines).

investigation is recommended to confirm this hypothesis.

CRediT authorship contribution statement

Mojtaba Mokhtari: Conceptualization, Methodology, Software, Formal analysis, Investigation, Data curation, Validation, Visualization, Resources, Project administration, Writing – original draft, Writing – review & editing. **Ekaterina Kim:** Conceptualization, Supervision, Resources, Project administration, Writing – review & editing. **Jørgen Amdahl:** Conceptualization, Supervision, Resources, Funding acquisition, Writing – review & editing.

Declaration of Competing Interest

The authors declare that they have no known competing financial interests or personal relationships that could have appeared to influence the work reported in this paper.

Data availability

Data will be made available on request.

Acknowledgements

The authors are grateful for the financial support of the Research Council of Norway through the Centers of Excellence funding scheme, project AMOS (grant number 223254) and the Centers for Research-based Innovation funding scheme, project CASA (grant number 237885), at the Norwegian University of Science and Technology.

References

[1] Shazly M, Prakash V, Lerch BA. High strain-rate behavior of ice under uniaxial compression. Int J Solids Struct 2009;46:1499–515.
[2] R. Ibrahim, N. Chalhoub, J. Falzarano, Interaction of ships and ocean structures with ice loads and stochastic ocean waves, (2007).
[3] Tippmann JD, Kim H, Rhymer JD. Experimentally validated strain rate dependent material model for spherical ice impact simulation. Int J Impact Eng 2013;57:43–54.
[4] Walker JD, Chocron S, Waite JH, Brockwell T. The vaporization threshold: hypervelocity impacts of ice grains into a titanium cassini spacecraft instrument chamber. Procedia Eng 2015;103:628–35.
[5] Wen K, Chen X-w, Lu Y-g. Research and development on hypervelocity impact protection using whipple shield: an overview. Defence Technol 2021;17:1864–86.
[6] Jordaan I. Some issues in ice mechanics. In: International conference on offshore mechanics and Arctic engineering. American Society of Mechanical Engineers; 2015. V008T007A027.
[7] Sinha NK. Short-term rheology of polycrystalline ice. J Glaciol 1978;21:457–74.
[8] Sinha NK. Rheology of columnar-grained ice. Exp Mech 1978;18:464–70.
[9] Sinha NK. Creep model of ice for monotonically increasing stress. Cold Reg Sci Technol 1983;8:25–33.
[10] Sinha NK. Crack-enhanced creep in polycrystalline material: strain-rate sensitive strength and deformation of ice. J Mater Sci 1988;23:4415–28.
[11] Xiao J, Jordaan I. Application of damage mechanics to ice failure in compression. Cold Reg Sci Technol 1996;24:305–22.
[12] Xiao J. Damage and fracture of brittle viscoelastic solids with application to ice load models. Memorial University of Newfoundland; 1997.
[13] Jordaan IJ, Matskevitch DG, Meglis IL. Disintegration of ice under fast compressive loading. Int J Fract 1999;97:279–300.
[14] Jordaan IJ. Mechanics of ice–structure interaction. Eng Fract Mech 2001;68:1923–60.
[15] Taylor RS. Analysis of scale effect in compressive ice failure and implications for design. Memorial University of Newfoundland; 2010.
[16] O'Rourke BJ, Jordaan IJ, Taylor RS, Gürtner A. Experimental investigation of oscillation of loads in ice high-pressure zones, part 1: single indentor system. Cold Reg Sci Technol 2016;124:25–39.
[17] Gagnon R, Gammon P. Triaxial experiments on iceberg and glacier ice. J Glaciol 1995;41:528–40.
[18] Michel B, Toussaint N. Mechanisms and theory of indentation of ice plates. J Glaciol 1977;19:285–300.
[19] Schulson EM. Brittle failure of ice. Eng Fract Mech 2001;68:1839–87.
[20] Jones SJ. A review of the strength of iceberg and other freshwater ice and the effect of temperature. Cold Reg Sci Technol 2007;47:256–62.
[21] Ince ST, Kumar A, Park DK, Paik JK. An advanced technology for structural crashworthiness analysis of a ship colliding with an ice-ridge: numerical modelling and experiments. Int J Impact Eng 2017;110:112–22.
[22] Ince ST, Kumar A, Paik JK. A new constitutive equation on ice materials. Ships Offshore Struct 2017;12:610–23.
[23] Cai W, Zhu L, Yu TX, Li Y. Numerical simulations for plates under ice impact based on a concrete constitutive ice model. Int J Impact Eng 2020;143:103594.
[24] Gupta V, Bergström JS. A progressive damage model for failure by shear faulting in polycrystalline ice under biaxial compression. Int J Plast 2002;18:507–30.
[25] Snyder SA, Schulson EM, Renshaw CE. Effects of prestrain on the ductile-to-brittle transition of ice. Acta Mater 2016;108:110–27.
[26] Mokhtari M, Kim E, Amdahl J. Pressure-dependent plasticity models with convex yield loci for explicit ice crushing simulations. Mar Struct 2022;84:103233.
[27] Jordaan IJ, Stone BM, McKenna RF, Fuglem MK. Effect of microcracking on the deformation of ice. Can Geotech J 1992;29:143–50.
[28] Dassault systèmes SIMULIA user assistance, Abaqus, (2019).
[29] Kim H, Daley C, Colbourne B. A numerical model for ice crushing on concave surfaces. Ocean Eng 2015;106:289–97.
[30] Kim J-H, Kim Y. Numerical simulation on the ice-induced fatigue damage of ship structural members in broken ice fields. Mar Struct 2019;66:83–105.
[31] Kim H, Quinton B. Evaluation of moving ice loads on an elastic plate. Mar Struct 2016;50:127–42.
[32] Zhou L, Wang F, Diao F, Ding S, Yu H, Zhou Y. Simulation of ice-propeller collision with cohesive element method. J Mar Sci Eng 2019;7:349.
[33] Kim J-H, Kim Y. Numerical simulation of concrete abrasion induced by unbreakable ice floes. Int J Naval Archit Ocean Eng 2019;11:59–69.
[34] Wang F, Zhou L, Zou Z-j, Song M, Wang Y, Liu Y. Study of continuous icebreaking process with cohesive element method. Brodogradnja: Teorija i praksa brodogradnje i pomorske tehnike 2019;70:93–114.
[35] Li H, Feng Y, Ong MC, Zhao X, Zhou L. An approach to determine optimal bow configuration of polar ships under combined ice and calm-water conditions. J Mar Sci Eng 2021;9:680.
[36] Kim J-H, Kim Y, Kim H-S, Jeong S-Y. Numerical simulation of ice impacts on ship hulls in broken ice fields. Ocean Eng 2019;182:211–21.
[37] Glen JW. The creep of polycrystalline ice. Proc R Soc Lond Ser A Math Phys Sci 1955;228:519–38.
[38] H. Dillon, O. Andersland, Physics of snow and ice (1967), Vol. I, 313-328.
[39] Gold LW. The failure process in columnar-grained ice. Canada: McGill University; 1970.
[40] Barnes P, Tabor D, Walker J. The friction and creep of polycrystalline ice. Proc R Soc Lond A Math Phys Sci 1971;324:127–55.
[41] Sinha NK, Ehrhart P, Carstanjen H, Fattah A, Roberto J. Grain boundary sliding in polycrystalline materials. Philos Mag A 1979;40:825–42.
[42] Jordaan IJ, McKenna RF. Constitutive relations for the creep of ice. In: Proceedings, international association for hydraulic research (IAHR) symposium on ice; 1988. p. 47–58.
[43] Jordaan IJ, McKenna RF. Modelling of progressive damage in ice. In: Proceedings, international association for hydraulic research (IAHR) symposium on ice; 1988. p. 582–624.
[44] R.A. Schapery, On viscoelastic deformation and failure behavior of composite materials with distributed flaws, 1981 advances in aerospace structures and materials, (1981) 5-20.
[45] Schapery RA. Correspondence principles and a generalizedJ integral for large deformation and fracture analysis of viscoelastic media. Int J Fract 1984;25:195–223.
[46] Xiao J. Finite element modelling of damage processes in ice-structure interaction. Memorial University of Newfoundland; 1991.
[47] Liu B. Numerical modelling of medium scale indentation tests. Memorial University of Newfoundland; 1994.
[48] Li C. Finite element analysis of ice-structure interaction with a viscoelastic model coupled with damage mechanics. MEng Dissertation, Memorial University of Newfoundland; 2002.
[49] Moore P, Jordaan I, Taylor R. Explicit finite element analysis of compressive ice failure using damage mechanics. In: Proceedings of the 22th international conference on port and ocean engineering under Arctic conditions; 2013. p. 9–13.
[50] Turner J. Constitutive behaviour of ice under compressive states of stress and its application to ice-structure interactions. Memorial University of Newfoundland; 2018.
[51] Jordaan IJ, McKenna RF. Processes of deformation and fracture of ice in compression. In: Proceedings IUTAM-IAHR symposium on ice-structure interaction. St. John's, Newfoundland, Canada: Springer; 1989. p. 283–309.
[52] Singh S, Jordaan I. Constitutive behaviour of crushed ice. Int J Fract 1999;97:171–87.
[53] Singh S, Jordaan I. Triaxial tests on crushed ice. Cold Reg Sci Technol 1996;24:153–65.
[54] Singh SK. Mechanical behaviour of viscoelastic material with changing microstructure. Memorial University of Newfoundland; 1993.
[55] R.F. McKenna, I.J. Jordaan, J. Xiao, Analysis of damage and energy flow in the crushed layer during rapid ice loading, in: Proceedings of IAHR symposium of ice, Espoo Finland, 1990, pp. 231-245.
[56] Jonas J, Muller F. Deformation of ice under high shear stress. Can J Earth Sci 1969;6.
[57] Kachanov M. Elastic solids with many cracks and related problems. Adv Appl Mech 1993;30:259–445.

[58] Shi C, Hu Z, Ringsberg J, Luo Y. A nonlinear viscoelastic iceberg material model and its numerical validation. Proc Inst Mech Eng Part M J Eng Marit Environ 2017; 231:675–89.
[59] Stone BM, Jordaan IJ, Jones SJ, McKenna RF. Damage of isotropic polycrystalline ice under moderate confining pressures. In: Proceedings of the 10th international conference on port and ocean engineering under Arctic conditions; 1989. p. 408–19. Lulea, Sweden.
[60] Xu Y, Hu Z, Ringsberg JW, Chen G. Nonlinear viscoelastic-plastic material modelling for the behaviour of ice in ice-structure interactions. Ocean Eng 2019; 173:284–97.
[61] Xu Y, Hu Z, Ringsberg JW, Chen G, Meng X. An ice material model for assessment of strain rate, temperature and confining pressure effects using finite element method. Ships Offshore Struct 2019;14:34–44.
[62] Meaney R, Jordaan I, Xiao J. Analysis of medium scale ice-indentation tests. Cold Reg Sci Technol 1996;24:279–87.
[63] Timco GW, Frederking RMW. Confined compression tests: outlining the failure envelope of columnar sea ice. Cold Reg Sci Technol 1986;12:13–28.
[64] Schulson EM. The brittle compressive fracture of ice. Acta Metall Mater 1990;38: 1963–76.
[65] Weiss J, Schulson EM. The failure of fresh-water granular ice under multiaxial compressive loading. Acta Metall Mater 1995;43:2303–15.
[66] Gratz E, Schulson E. Brittle failure of columnar saline ice under triaxial compression. J Geophys Res: Solid Earth 1997;102:5091–107.
[67] Sammonds P, Murrell S, Rist M. Fracture of multiyear sea ice. J Geophys Res: Oceans 1998;103:21795–815.
[68] Schulson EM, Gratz ET. The brittle compressive failure of orthotropic ice under triaxial loading. Acta Mater 1999;47:745–55.
[69] Iliescu D, Schulson EM. The brittle compressive failure of fresh-water columnar ice loaded biaxially. Acta Mater 2004;52:5723–35.
[70] Golding N, Schulson EM, Renshaw CE. Shear faulting and localized heating in ice: the influence of confinement. Acta Mater 2010;58:5043–56.
[71] Sain T, Narasimhan R. Constitutive modeling of ice in the high strain rate regime. Int J Solids Struct 2011;48:817–27.
[72] A. Derradji-Aouat, A unified failure envelope for isotropic fresh water ice and iceberg ice, in: Proceedings of ETCE/OMAE joint conference energy for the new millenium, 2000.
[73] A. Derradji-Aouat, Explicit FEA and constitutive modelling of damage and fracture in polycrystalline ice-simulations of ice loads on structures, in: Proceedings of 18th international conference on port and ocean engineering under Arctic conditions, I, 2005, pp. 225-238.
[74] A. Derradji-Aouat, E. Evgin, Progressive damage mechanism for ductile failure for polycrystalline ice and its complementary brittle failure criterion, OMAE-2001, Rio de Janeiro, Brazil. Polar and Arctic session, PDF file, 6002 (2001).
[75] Derradji-Aouat A. Multi-surface failure criterion for saline ice in the brittle regime. Cold Reg Sci Technol 2003;36:47–70.
[76] Derradji-Aouat A, Sarzynski M, Cordes R. Iceberg ice constitutive modeling and FEA validation. In: OTC Arctic technology conference. OnePetro; 2015.